



LES study on turbulent dust deposition and its dependence on atmospheric boundary-layer stability

Xin Yin¹, Cong Jiang¹, Yaping Shao¹, Ning Huang², Jie Zhang²

¹ Institute for Geophysics and Meteorology, University of Cologne, Cologne, Germany

5 ² Key Laboratory of Mechanics on Disaster and Environment in Western China, Lanzhou University, Lanzhou, China

Correspondence to: Jie Zhang (zhang-j@lzu.edu.cn)

Abstract. It is increasingly recognized that atmospheric boundary-layer stability (ABLS) plays an important role in aeolian processes. While the effects of ABLS on dust emission have been documented in several studies, those on dust deposition are less well studied. By means of large-eddy simulation, we investigate how ABLS influences the probability distribution of surface shear stress and hence dust deposition. Statistical analysis of the model results reveals that the shear stress can be well approximated by using a Weibull distribution and the ABLS influences on dust deposition can be estimated by considering the shear stress fluctuations. The model-simulated dust depositions are compared with the predictions of a dust-deposition scheme and measurements, and the findings are then used to improve the dust-deposition scheme. This research represents a further step towards developing dust schemes that account for the stochastic nature of dust processes.

Keywords: Dust deposition, Atmospheric boundary-layer stability, Surface shear stress, Weibull distribution, Stochastic dust process

20 1 Introduction

Dry deposition is the removal of particulates and gases at the air-surface interface by turbulent transfer and gravitational settling (Sehmel, 1980; Droppo, 2006; Hicks et al., 2016). Because it is the only process for the removal of particles from the atmosphere in the absence of precipitation, developing reliable methods for estimating dry deposition of particles has attracted much interest since the early 1940s (Gregory, 1945; Chamberlain, 1953; Slinn and Slinn, 1980; Slinn, 1982; Zhang et al., 2001; Petroff and Zhang, 2010; Zhang and Shao, 2014; Seinfeld et al., 2016). Several particle-deposition schemes have been proposed (e.g., Slinn, 1982; Zhang and Shao, 2014) for regional/global models, which are driven by using several environmental parameters, including the Reynolds surface shear stress (typically averaged over 15–30 min). However, field observations indicate that the use of Reynolds stress as the only wind-related parameter in such schemes may not be sufficient to achieve accurate estimates of particle deposition, because of the nonlinear relationship between deposition velocity and wind shear. The observations using the eddy correlation method show that particle-deposition velocity has strong spatiotemporal variations associated with the fluctuations of wind speed (Connan et al., 2018; Damay et al., 2009; Lamaud et al., 1994; Wesely et al., 1983, 1985). It is also



35 observed that when the background wind speeds are similar, deposition velocity under convective conditions is in general larger than under neutral and stable conditions. Pellerin et al. (2017) suggested that cospectral similarities exist between heat and particle-deposition fluxes and that atmospheric turbulence plays a role in dust deposition. It is therefore necessary to find a link between instantaneous wind and particle deposition and to correctly represent this link in particle-deposition schemes, i.e., to introduce and account for the effect of turbulence on particle deposition.

40 Models for turbulent dust emission (Klose and Shao, 2012, 2013) and sand saltation (Liu et al., 2018; Li et al., 2020; Rana et al., 2020) have been developed, but to our knowledge, although turbulent dust deposition is now perceived to be important, a scheme is yet to be constructed for its quantitative estimate.

45 The turbulent wind flow in a particle-deposition scheme is reflected in the turbulent shear stress (or vertical momentum flux). It is well-known that apart from gravitational settling, particle deposition is driven by turbulent diffusion which is intimately related to the vertical momentum transfer in the atmospheric boundary layer (ABL) (Wyngaard, 2010). Based on the Prandtl mixing-length theory, the shear stress can be parameterized in neutral conditions. However, it is known that for a given mean wind speed (at a reference height) in the ABL, both the mean value and the perturbations of shear stress depend on the atmospheric boundary-layer stability (ABLS), for instance, shear stress shows generally larger fluctuations in convective

50 ABLS. Klose and Shao (2012) pointed out that, under convective conditions, large eddies have coherent structures of dimensions comparable to boundary-layer depth, which are efficient entities in generating localized momentum fluxes to the surface. Although the eddies only occupy fractions of time and space, the momentum fluxes to these fractions can be many times the average. Hicks et al. (2016) mentioned that ABLS is of immediate concern in the micrometeorological community, because of its influences on the intermittency, gustiness and diurnal cycle of particle deposition. Similar to dust emission and sand saltation,

55 intermittent dust deposition also occurs as a result of fluctuating surface shear stress. The current particle-deposition schemes only consider the mean behavior of wind, and how this mean behavior varies with ABLS via the Monin-Obukhov similarity theory, (Monin et al., 2007; Monin and Obukhov, 1954), but not the fluctuations of the associated shear stress and how they vary with ABLS.

60 We argue that focusing only on the effects of ABLS on mean wind is insufficient to model particle deposition accurately. In this study, we explore the influences of ABLS on the turbulent behavior of particle deposition and attempt to improve an existing particle deposition scheme. A large-eddy simulation (LES) model is used to simulate turbulence and particle deposition under various ABLS conditions. The dust particle depositions simulated using the LES model and predicted using the particle-deposition scheme of Zhang and Shao (2014, ZS14 hereafter) are compared with each other and with measurements. Here, we address the following three issues: (1) How ABLS affects the probability distribution of surface shear stress; (2) How ABLS impacts on particle deposition; and (3) How the ZS14 scheme can be improved to account for the ABLS effect. On this basis, an improvement to the ZS14 scheme (also applicable to other schemes) is proposed. The remaining part of the paper is organized as follows: Sect. 2 gives a brief description of the Weather Research and

65



70 Forecast – Large-Eddy Simulation Model with Dust module (WRF-LES/D), the ZS14 scheme, and the design of the numerical experiments. Sect. 3 discusses the findings of the numerical simulations and the improvement to the ZS14 scheme. The concluding remarks are given in Sect. 4.

2. Model/Method

2.1 WRF-LES/D

75 The WRF-LES/D used here is initially developed by Shao et al. (2013) and Klose and Shao (2013) by coupling the WRF-LES (Moeng et al., 2007; Skamarock et al., 2008) with a land-surface module and dust module. As demonstrated in the earlier studies, WRF-LES/D is a reasonably well-established system for applications to simulating turbulence, turbulent dust emission and transport for various ABL conditions. WRF-LES is a three-dimensional and non-hydrostatic model for fully compressible flow. The model
 80 separates the turbulent flow into a grid-resolved component and a subgrid component. The $k-l$ subgrid closure (Deardorff, 1980) together with the TKE equation (Skamarock et al., 2008) based on nonlinear backscatter and anisotropic (Kosović, 1997; Mirocha et al., 2010) are used here. The governing equations in WRF-LES/D include the equations of motion, continuity equation, enthalpy equation, equation of state and the dust conservation equation, as shown below

$$85 \quad \frac{\partial u_i}{\partial t} + \frac{\partial u_i u_j}{\partial x_j} = -\delta_{i3} g + \varepsilon_{ij3} f u_j - \frac{1}{\rho_a} \frac{\partial p}{\partial x_i} + \nu \frac{\partial^2 u_i}{\partial x_j \partial x_j} - \frac{1}{\rho_a} \frac{\partial \tau_{ij}}{\partial x_j} \quad (1)$$

$$\frac{\partial \rho_a}{\partial t} + \frac{\partial (\rho_a u_j)}{\partial x_j} = 0 \quad (2)$$

$$\frac{\partial c_p T}{\partial t} + \frac{\partial (c_p u_j T)}{\partial x_j} = \frac{\partial H_j}{\partial x_j} + s_r \quad (3)$$

$$p = \rho_a R_a T \quad (4)$$

$$\frac{\partial c}{\partial t} + u_j \frac{\partial c}{\partial x_j} - w_t \frac{\partial c}{\partial z} = -\frac{\partial F_j}{\partial x_j} + s_r \quad (5)$$

90 where u_i (u, v, w) is grid-resolved flow velocity along x_i (x, y, z) refer to the streamwise, spanwise, and vertical directions, respectively; g is the acceleration due to gravity; ρ_a is the air density; f is the Coriolis parameter; p is pressure; τ_{ij} is subgrid stress tensor modeled using an eddy viscosity approach where the eddy viscosity is represented as the product of a length scale and a velocity scale characterizing the subgrid-scale (SGS) turbulent eddies, with the velocity scale being derived from the SGS TKE and the length scale
 95 from the grid spacing; ν is the kinematic viscosity; δ_{ij} is the Kronecker operator and ε_{ij} is the alternating operator; c_p is the specific heat of air at constant pressure; T is air temperature; H_j is the j th component of subgrid heat flux; c is dust concentration; w_t is dust particle terminal velocity; F_j is the j th component of subgrid dust flux; s_r and s_r are the source or sink terms for heat and particles, respectively. The eddy



diffusivity is obtained using eddy viscosity dividing the Prandtl number. For the surface layer, an important
100 parameterization to solve the governing equations for high-Reynolds-number turbulence is embedded in the
surface boundary condition, which computes the instantaneous local surface shear stress using the bulk
transfer method (Kalitzin et al., 2008; Kawai and Larsson, 2012; Piomelli et al., 2002; Zheng et al., 2020) as
follows,

$$\tau = \rho_a K_m \frac{\partial V}{\partial z} \quad (6)$$

105 with

$$K_m = \frac{ku_* z}{\varphi_m} \quad (7)$$

where K_m being eddy viscosity and φ_m being the MOST stability function, $V = \sqrt{u^2 + v^2}$. Even though
Shao et al. (2013) questioned the application of the MOST in LES, it is still used here, as our emphasis is on
the variance of shear stress in the simulation domain. Several land-surface models (LSMs) can be selected
110 (e.g., Chen and Dudhia, 2000; Pleim and Xiu, 2003) in WRF-LES/D, and the 5-layer thermal diffusion
(Dudhia, 1996) is used in this study. Surface heat flux in this study is artificially given. In addition, we denote
surface heat flux as H_0 and dust dry deposition flux on grand in each grid as F_d .

2.2 Particle-deposition scheme of ZS14

The dust particle deposition on the surface is more complicated than momentum flux as the dust concentration
115 changing close to the surface is unclear. To solve the dust conservation equation, Eq. (5), the emission and
deposition fluxes at the surface need to be specified. The problem of dust emission has been dealt with
elsewhere (Shao, 2004; Klose and Shao, 2013) and is not considered here. For our purpose, dust emission is
assumed to be zero. This section gives the parameterization scheme of surface settlement proposed by ZS14.
The detail of the scheme is as described in ZS14, only the main results are given here for completeness. In
120 general, we can express dust deposition flux F_d as

$$F_d = -\left(K_p + k_p\right) \frac{\partial c}{\partial z} - w_t \cdot c \quad (8)$$

where K_p and k_p are eddy diffusivity and molecular diffusivity, respectively. By analogy with the bulk-transfer
formulation of scalar fluxes in ABL, F_d can be parameterized as

$$F_d = -V_d(z) \cdot c(z) \quad (9)$$

125 where $c(z)$ is the dust concentration at height z (the center height of the lowest model level in this study),
 $V_d(z)$ is the corresponding dry deposition velocity.

The surface layer is divided into an inertial layer and a roughness layer. Integrating Eq. (8) in inertial layer
and substitute Eq. (9) into it, $V_d(z)$ is obtained:



$$V_d(z) = \left(r_g + \frac{r_s - r_g}{\exp(r_a / r_g)} \right)^{-1} \quad (10)$$

130 with r_a being the aerodynamic resistance for the inertial layer. Using the MOST, we have

$$r_a = \frac{S_{cT}}{\kappa u_*} \left[\ln \left(\frac{z - z_d}{h - z_d} \right) - \psi_m \right] \quad (11)$$

where z_d is the displacement height, h is the height of roughness element ψ_m is the integral of stability function in the inertial layer, $S_{cT} = K_m / K_p$ (Csanady, 1963), and κ is the von Karman constant. The gravitational resistance r_g is defined as the reciprocal of the gravitational settling and depends mainly on particle size and density. A free-falling particle is subject to gravitational and aerodynamic drag forces. When these forces are in equilibrium, the gravitational settling velocity reaches the terminal velocity given by the Stokes formula

$$w_t = \frac{C_u \rho_p D_p^2 g}{18 \mu_a} = r_g^{-1} \quad (12)$$

where D_p is the particle diameter, ρ_p is the particle density, μ_a is the air dynamic viscosity, C_u is the Cunningham correction factor that accounts for the slipping effect affecting the fine particles.

140 In the roughness layer, the collection process is reflected in collection resistance, defined by $r_s = -\frac{c(h)}{F_d}$ with an assumption of dust concentration is zero on roughness elements or ground. In addition to the meteorological factors and land-use category, Zhang and Shao (2014) established a relationship between aerodynamic and surface-collection processes by using an analogy between drag partition and deposition flux partition, which can describe surface heterogeneity.

$$145 \quad r_s^{-1} = R \cdot \frac{\tau}{\rho_d u_h} \left(\frac{E \tau_c}{C_d \tau} + \left(1 + \frac{\tau_c}{\tau} \right) S_c^{-1} + 10^{-\frac{3}{\hat{T}}} \right) + w_t \quad (13)$$

Here, R is the reduction of collection caused by particle rebound, E is the collection coefficient of the roughness elements, which includes the contributions of Brownian motion, impaction and interception, S_c is the Schmidt number which is the ratio of air viscosity to molecular diffusion, u_h is the wind speed at the top of roughness layer, C_d is the drag coefficient for isolated roughness element, $10^{-\frac{3}{\hat{T}}}$ represents the turbulent impaction efficiency with \hat{T} being the dimensionless particle relaxation time. The ratio τ_c / τ describes the drag partition with τ_c being the pressure drag (the force exerted on roughness elements) and can be calculated according to Yang and Shao (2006) as



$$\frac{\tau_c}{\tau} = \frac{\beta \lambda_e}{1 + \beta \lambda_e} \quad (14)$$

and

$$155 \quad \lambda_e = \frac{\lambda}{(1-\eta)^6} \cdot \exp\left(-\frac{\lambda}{10 \cdot (1-\eta)^6}\right) \quad (15)$$

with β ($= 200$) is the ratio of the pressure drag coefficient for isolated roughness element to that of bare surface, λ is the frontal area index of the roughness elements, η is the basal area index or the fraction of cover. From Eqs. (10)-(15), it can be seen that V_d and τ are nonlinearly related. As example, for the particle of diameter $1 \mu\text{m}$, analysis shows that when τ is small, V_d is dominated by w_t . As τ increases, w_t and τ are both
160 important in V_d . As τ increases further, the effect of τ becomes much larger than gravity settling, thus the V_d is mainly determined by τ .

2.3 Simulation Set-up

Numerical experiments are carried out with WRF-LES/D for various atmospheric stability and background-wind conditions for two different roughness lengths (Table 1). The domain of the simulation is
165 $2000 \times 2000 \times 1500 \text{ m}^3$ and the number of grid points is $200 \times 200 \times 90$ corresponding to a horizontal resolution $\Delta x = \Delta y = 10 \text{ m}$. The Arakawa-C staggered grid is used. The depth of the lowest model layer is 1 m and the grid above is stretched following a logarithmic function of z . The simulation time is 90 minutes with a time step of 0.05 s and the output interval is 10 s . The first 30 minutes of the simulation is the model spin-up time and the data of the remaining 60 minutes are used for the analysis.

170 For model initialization, the wind and dust concentration (Chamberlain, 1967; Monin, 1970; Kind, 1992) are assumed to be logarithmic in the vertical and uniform in the horizontal direction. For each experiment, a constant surface heat flux is specified. A 300 m deep Rayleigh damping layer is used at the upper boundary with a damping coefficient of 0.01 . The wind speed at the top boundary, U , is given in Table 1. The surface heat flux, H_0 , increases from -50 to 600 W m^{-2} , and for each surface heat flux, the wind conditions increase
175 from 4 to 16 m s^{-1} in Exp (1-20) and from 5.44 to 18.12 m s^{-1} in Exp (21-35). The roughness length z_0 for sand surface used in Exp (1-20) is 0.153 mm following wind tunnel experiment (Zhang and Shao, 2014) but 0.76 mm in Exp (21-35) according to field observation (Bergametti et al., 2018). The lateral boundary conditions are periodic, which allows the simulation of a well-developed boundary layer. The vertical scaling

velocity is estimated using heat flux, $w_* = \left(\frac{g}{\bar{\theta}} \frac{H_0}{\rho_a c_p} z_l\right)^{1/3}$, with $\bar{\theta}$ being the mean potential temperature

180 and $z_l = 1000 \text{ m}$ is the boundary layer inversion height. Usually, w_* is not used for stable ABLs, but used here as an indicator for the suppression of turbulence by negative buoyancy.



Table 1: List of numerical experiments with $z_0 = 0.153$ mm for Exp (1-20) in wind tunnel experiments (Zhang and Shao, 2014) and $z_0 = 0.76$ mm for Exp (21-35) in field observation (Bergametti et al., 2018) for sand surface.

$z_0 = 0.153$ mm		$z_0 = 0.76$ mm		H_0 (W m ⁻²)	w^* (m s ⁻¹)
NAME	U (m s ⁻¹)	NAME	U (m s ⁻¹)		
EXP1	4	EXP21	5.44	-50	-1.12
EXP2	8	EXP22	10.87	-50	-1.12
EXP3	12	EXP23	18.12	-50	-1.12
EXP4	16	--	--	-50	-1.12
EXP5	4	EXP24	5.44	0	0
EXP6	8	EXP25	10.87	0	0
EXP7	12	EXP26	18.12	0	0
EXP8	16	--	--	0	0
EXP9	4	EXP27	5.44	200	1.77
EXP10	8	EXP28	10.87	200	1.77
EXP11	12	EXP29	18.12	200	1.77
EXP12	16	--	--	200	1.77
EXP13	4	EXP30	5.44	400	2.23
EXP14	8	EXP31	10.87	400	2.23
EXP15	12	EXP32	18.12	400	2.23
EXP16	16	--	--	400	2.23
EXP17	4	EXP33	5.44	600	2.55
EXP18	8	EXP34	10.87	600	2.55
EXP19	12	EXP35	18.12	600	2.55
EXP20	16	--	--	600	2.55

3. Results

185 3.1 Turbulent shear stress

In the first set of the analysis, we examine the impact of atmospheric stability on shear stress fluctuations. Early dust deposition studies considered only the time average of surface shear stress, τ_r , with the assumption that shear stress is horizontally homogeneous. In WRF-LES/D, the corresponding mean resultant shear stress τ_r can be obtained as below:

$$190 \quad \tau_r = \sqrt{\overline{\tau_{xz}^2} + \overline{\tau_{yz}^2}} \quad (16)$$

The shorthand notation $\bar{f} = \frac{1}{N_x N_y N_t} \sum_{n_x, n_y, n_t} f(n_x, n_y, n_t)$ is introduced to represent the space and time average over the simulation domain and time period (hereafter ensemble mean) with N_x (=200) and N_y (=200) are the numbers of grid points in the x - and y -direction, respectively, and N_t (=360) the time steps of model output.

195 Figure 1a-c show the instantaneous shear stress, τ , of a sample grid ($n_x = 198$, $n_y = 41$) over a one-hour period for the runs with $z_0 = 0.153$ mm, $U = 4$ m s⁻¹ and various ABL stabilities ($H_0 = 0, 200, 600$ W m⁻²). Figure 1d-f is same as Fig. 1a-c, but for $U = 16$ m s⁻¹. The panel shows that τ is not a constant, and the mean resultant shear stress, as well as the shear stress fluctuations, increase with increasing atmospheric instability. In



200 addition, the insert plots in Fig. 1 show that the autocorrelation function, ACF, is oscillated during decrease. The oscillation periodicity is longer under weak wind conditions (Fig. 1a-c) than strong wind (Fig. 1d-f). The ACF in neutral conditions decreases rapidly than in convective conditions. Recall the definition of coherent motion given by Robinson (1991) - the correlation of variables over a range of long time larger than the smallest scales of flow is an evidence of coherent oscillating motion. Thus, the regular oscillation and a long time correlation of τ are closely related to the evolution of the coherent structure. This indicates that in a convective ABL, stronger large-scale coherent structures exist even under weak wind conditions.

205 To gain insight into the behavior of the unsteady shear stress field, we introduce the turbulence intensity of surface shear stress (TI-S) defined as the ratio of the standard deviation of fluctuating surface shear stress, σ_τ , to the mean resultant stress τ_r , i.e., σ_τ/τ_r . Analysis shows that σ_τ/τ_r increases as atmospheric conditions become more unstable and decreases with wind speed (e.g., Fig. 1). High wind speeds tend to force the ratio to be more similar to that in neutral ABLs, as the mean-wind induced shear stress becomes dominant over the large-eddy induced shear-stress fluctuations. For a weak TI-S, τ is dominated by τ_r , and the stress fluctuations are small compared to τ_r . As TI-S increases, the contribution of momentum transport by large eddies becomes significant because in unstable ABLs, buoyancy generated large eddies penetrate to high levels and intermittently enhance the momentum transfer to the surface.

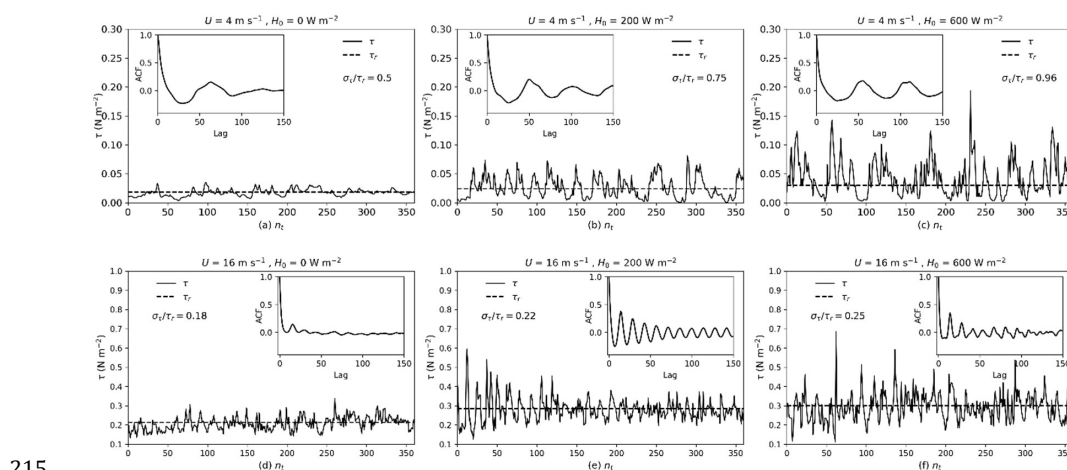


Figure 1. Time evolutions of surface shear stress τ with different H_0 values and $z_0 = 0.153$ mm at the grid point $n_x = 198$ and $n_y = 41$ (a-c) for $U = 4$ m s⁻¹; (d-f) for $U = 16$ m s⁻¹; the insert plots are the autocorrelation functions of τ .

220 The intermittent surface shear stress can directly cause localized dust deposition. Therefore, dust deposition is also intermittent in space and time. However, to our knowledge, in existing dust-deposition schemes (e.g., ZS14 used here), the dust-deposition velocity is calculated using only the mean resultant shear stress τ_r instead of the instantaneous shear stress. We denote this deposition velocity as V_{d,τ_r} . The mean deposition



velocity simulated by WRF-LES/D, denoted as $V_{d,LES}$, is estimated via the ratio of the ensemble mean of dust deposition flux and the ensemble mean of dust concentration:

$$V_{d,LES} = -\frac{\overline{F}_d}{\overline{c}} \quad (17)$$

225 which is consistent with the methods commonly used in field observations and wind-tunnel experiments. Figures 2a and 2b, with the same wind conditions as for Fig. 1a-c and 1d-f, show the time evolution of the instantaneous deposition velocity V_d for particles of diameter $1.46 \mu\text{m}$ and surface heat flux $H_0 = 600 \text{ W m}^{-2}$. As shown, the fluctuation behavior of V_d is consistent with that of τ . Moreover, Fig. 2a shows a substantial difference between $V_{d,LES}$ and V_{d,τ_r} , while Fig. 2b shows V_{d,τ_r} is similar with $V_{d,LES}$. This suggests that the
 230 ZS14 scheme can more accurately estimate the deposition velocity for weak TI-S but underestimates the deposition velocity for strong TI-S. The reason for this is that in the case of strong TI-S, dust deposition caused by the gusty wind plays an important role as V_d and τ are non-linearly related, which is not reflected in V_{d,τ_r} . Since τ fluctuates and sometimes strongly, a bias always exists in conventional dust-deposition schemes and the magnitude of the bias depends on turbulence intensity. Therefore, in order to estimate dust
 235 deposition accurately, we need to first describe and parameterize the shear stress.

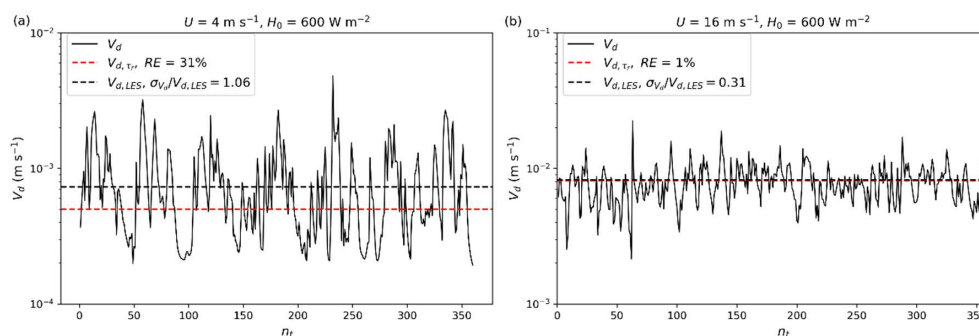


Figure 2. Time evolutions of deposition velocity V_d at grid point $n_x = 198$, $n_y = 41$ when $H_0 = 600 \text{ W m}^{-2}$, $z_0 = 0.153 \text{ mm}$ and (a) $U = 4 \text{ m s}^{-1}$ and (b) $U = 16 \text{ m s}^{-1}$. $RE = \left| \frac{V_{d,LES} - V_{d,\tau_r}}{V_{d,LES}} \right| \times 100\%$ is the relative error between V_{d,τ_r} and $V_{d,LES}$, $\sigma_{V_d}/V_{d,LES}$ is the ratio of the standard deviation of simulated instantaneous deposition velocity V_d and mean deposition velocity, $V_{d,LES}$.

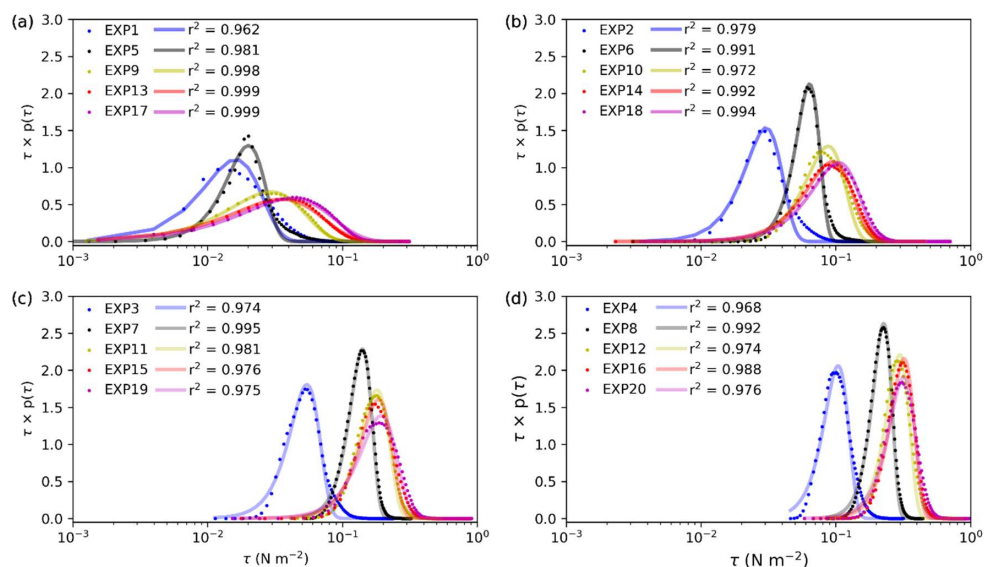
240 As a main predisposing factor for aeolian processes, turbulent shear stress has attracted much attention (e.g., Klose et al., 2014; Li et al., 2020a; Liu et al., 2018; Rana et al., 2020; Zheng et al., 2020). Similar to previous studies, we use the probability density function $p(\tau)$ to characterize the stochastic variable τ . Figure 3 shows that the variability of τ increases as atmospheric instability increases. The statistic moments of τ , including
 245 its mean resultant value τ_r , standard deviation σ_τ , skewness γ_1 of Exp (1-20) are listed in Table 2. σ_τ and τ_r increases with increased instability, and the distribution is positively skewed. Positive skewness is characterized by the distribution having a longer positive tail as compared with the negative tail and the



250 distribution appears as a left-leaning (i.e., tends toward low values) curve. This indicates that large negative fluctuations are not as frequent as large positive fluctuations. The data also shows γ_l generally shows a downward trend as TI-S decreases, which is consistent with (Monahan, 2006), i.e., as TI-S decreases, $p(\tau)$ becomes increasingly Gaussian.

Table 2. Statistics of shear stress for numerical experiments Exp (1-20).

NAME	H_0	U	τ_r	σ_τ	σ_τ/τ_r	γ_l	α	β
EXP1	-50	4	0.0156	0.0086	0.554	1.902	2.026	0.011
EXP2		8	0.0295	0.0096	0.327	1.573	3.154	0.023
EXP3		12	0.0524	0.0115	0.22	1.029	3.923	0.044
EXP4		16	0.1009	0.0158	0.157	0.835	4.819	0.09
EXP5	0	4	0.0185	0.0093	0.5	1.896	3.049	0.017
EXP6		8	0.0604	0.0151	0.25	1.142	5.004	0.055
EXP7		12	0.1315	0.0266	0.202	0.166	5.383	0.122
EXP8		16	0.2136	0.038	0.178	0.087	6.191	0.196
EXP9	200	4	0.024	0.018	0.75	1.142	1.56	0.025
EXP10		8	0.0812	0.0325	0.4	1.02	3.022	0.076
EXP11		12	0.1676	0.0451	0.269	0.512	4.078	0.156
EXP12		16	0.2848	0.0624	0.219	0.766	5.214	0.259
EXP13	400	4	0.026	0.0248	0.955	1.127	1.302	0.03
EXP14		8	0.0825	0.0372	0.451	0.646	2.513	0.081
EXP15		12	0.1728	0.0522	0.302	0.677	3.776	0.160
EXP16		16	0.2992	0.0646	0.216	0.289	5.214	0.278
EXP17	600	4	0.0299	0.0287	0.96	1.083	1.303	0.035
EXP18		8	0.0894	0.0424	0.474	0.715	2.472	0.089
EXP19		12	0.1767	0.0604	0.342	0.614	3.252	0.167
EXP20		16	0.3003	0.0739	0.246	0.511	4.493	0.277



255

Figure 3. Probability density functions derived from WRF-LES/D simulated surface shear stress (dots) and the corresponding fitted Weibull density functions (solid lines, r^2 is the coefficients of determination) for different surface heat fluxes and different wind speeds: (a) $U = 4 \text{ m s}^{-1}$, (b) $U = 8 \text{ m s}^{-1}$, (c) $U = 12 \text{ m s}^{-1}$, (d) $U = 16 \text{ m s}^{-1}$ with $z_0 = 0.153 \text{ mm}$.

260 The parameterization of surface shear stress has attracted intense interests, as example, Klose et al. (2014) reported that τ in unstable conditions is Weibull distributed based on large-eddy simulations. Shao et al. (2020) found that $p(\tau)$ is skewed to small τ values (i.e., positively skewed) based on field observations. Li et al. (2020) suggested that τ in neutral conditions is Gauss distributed based on a wind-tunnel experiment. Colella and Keith (2003) explained that in turbulent shear flows, the non-linear interaction between the eddies gives rise to a departure from Gaussian behavior. Our results show that the Gaussian approximation is inadequate in representing the skewed $p(\tau)$, especially for the conditions of strong turbulence intensity (e.g., unstable cases in Fig. 3a). Therefore, $p(\tau)$ here is approximated using a Weibull distribution, i.e.,

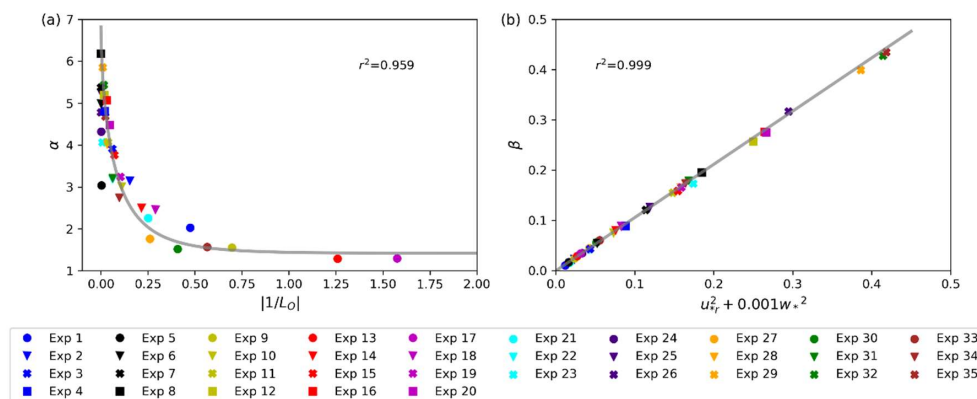
$$p(\tau) = \frac{\alpha}{\beta} \left(\frac{\tau}{\beta} \right)^{\alpha-1} \exp\left(-(\tau/\beta)^\alpha\right) \quad (18)$$

270 where α and β are the shape and scale parameters, respectively. The values of α and β for the numerical experiments Exp (1-20) are listed in Table 2. It can be seen that both α and β depend on wind speed and atmospheric stability. However, β is mainly determined by wind conditions when wind is strong, while it is affected by ABL stability when wind is weak. The behavior of α and β are shown in Fig. 4. In both stable and unstable atmospheric conditions, analysis shows that the scale parameter α is related to ABL stability as the power of $|1/L_o|$ where L_o is the Monin-Obukhov length. Fig. 4a shows that α decreases with the $|1/L_o|$, satisfying approximately Eq. (19). For neutral conditions, L_o goes to infinity, Eq. (19) no longer applies. Therefore, the shape parameter obtained by the fitting was directly used for pdf reproduction for the neutral

275



cases instead of the approximated α used for stable and unstable conditions. As Fig. 4b shows, the β parameter increases almost linearly with $u_{*r}^2 + 0.001 \cdot w_*^2$ but can be best approximated using Eq. (20) with $u_{*r} = \sqrt{\tau_r / \rho_a}$.



280

Figure 4. (a) Dependency of the shape parameter α on L_o^{-1} for all numerical experiments Exp (1-35); (b) Dependency of scaling parameter β on $(u_{*r}^2 + 0.001w_*^2)$ for Exp (1-35).

$$\alpha = 5.39 \cdot \exp \left(-5.43 \left(\frac{1}{L_o} \right)^{2/3} \right) + 1.42 \quad (19)$$

$$\beta = 1.058 \cdot (u_{*r}^2 + 0.001w_*^2) \quad (20)$$

285 Using Eqs. (18)-(20), we can approximately describe the turbulent surface shear stress in non-neutral cases.

3.2 Improvement to dust deposition scheme

Figure 5a shows the performances of WRF-LES/D by comparing the simulated deposition velocity, $V_{d,LES}$, with wind tunnel experiments (Zhang and Shao, 2014) and field observation (Bergametti et al., 2018). The observed data are measured under neutral conditions and similar wind flow. As shown, the simulation results agree well with the observed data. On this basis, we further evaluate the performance of the ZS14 scheme, and show that the accuracy of ZS14 scheme decreases as instability increases. As examples, Fig. 5b compared $V_{d,LES}$, of Exp (5, 9, 17) and Exp (24, 27, 33) with the ZS14 scheme result V_{d,τ_r} which is calculated using τ_r . It shows that under weak wind conditions, V_{d,τ_r} predicts the deposition well under neutral conditions and underestimates the deposition under convective conditions, especially for particles that are not dominated by molecular diffusion and gravity, and the underestimation increases with the atmospheric instability. To predicts the deposition velocity more accurately for convective conditions, we need to account for the effect of shear-stress fluctuations, i.e., the instantaneous shear stress distribution. Thus, the dry deposition scheme can be improved as

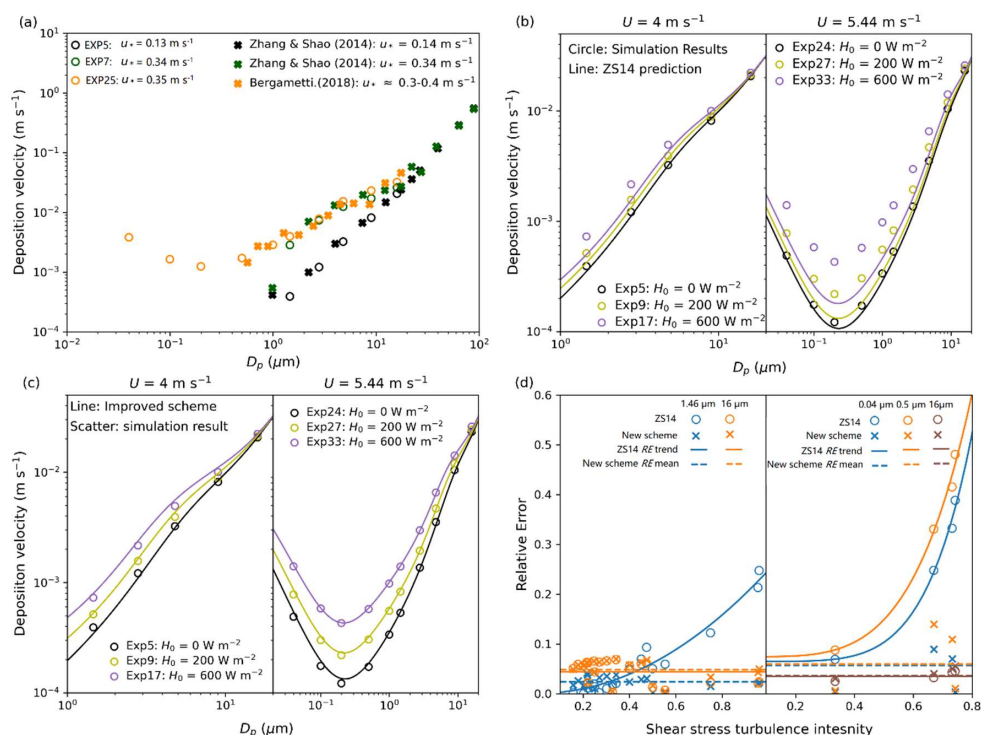
290

295



$$V_{d,\tau} = \int_0^{\infty} V_d(\tau) p(\tau) d\tau \quad (21)$$

300 with $p(\tau)$ is as given by Eqs. (18)-(20). As Fig. 5c shows, the improved scheme results $V_{d,\tau}$ and the simulation value $V_{d,LES}$ are shown a remarkable congruence.



305 **Figure 5.** (a) Validation of the simulated deposition velocity from WRF-LES/D (circles) by comparing with the observation data (crosses). (b) the comparison of the predicted result by ZS14 scheme (lines) with the simulated value (circles) of Exp (5, 9, 17) (left) and Exp (24, 27, 33) (right). (c) the comparison of the predicted result by the improved scheme (lines) with the simulated value (circles) of Exp (5, 9, 17) (left) and Exp (24, 27, 33) (right). (d) Comparison of relative error as a function of shear stress turbulence intensity (TI-S), estimated by ZS14 scheme (circles) and the improved scheme (crosses) for Exp (1-20) (Left) and Exp (24, 27, 30, 33) (right).

310 To make the comparison more clear, the relative errors (RE) of the predicted deposition velocity by ZS14 scheme and improved scheme are compared with the WRF-LES/D simulation value and are calculated as below

$$RE = \left| \frac{V_{d,LES} - V_{d,\tau} \text{ (or } V_{d,\tau})}{V_{d,LES}} \right| \times 100\% \quad (22)$$

315 Analysis shows that the value of relative error, RE , depends on surface conditions, wind conditions, atmospheric stabilities, and particle sizes. It increases obviously with increased atmospheric instability under



weak wind conditions, while becomes less sensitive to stability when wind is strong. Through the analysis, we find that the RE of ZS14 scheme generally increases with the shear stress turbulence intensity, TI-S, and the value depends on particle size, as shown in Fig. 5d (left). Thus, we compared the RE of some different sized particles to investigate that the particle in which size range is strongly affected (Fig. A2). The result
320 shows that RE first increases and then decreases with increasing particle size, and the particles with size normally in the range of 0.01 to 10 are strongly affected by turbulent shear stress and $p(\tau)$ needs to be considered. After modification, the errors are limited to less or about 10%. For example, the relative error of Exp (17, i.e., $U = 4 \text{ m s}^{-1}$ and $H_0 = 600 \text{ W m}^{-2}$) for particles of $1.46 \mu\text{m}$ is reduced from $\sim 25\%$ to $\sim 3\%$. The relative error of Exp (33, i.e., $U = 5.44 \text{ m s}^{-1}$ and $H_0 = 600 \text{ W m}^{-2}$) for particles of $0.5 \mu\text{m}$ is reduced from \sim
325 50% to $\sim 12\%$.

To further analyze if the RE of ZS14 in unstable conditions is dominated by kinetic instability or dynamic instability, the Richardson number is calculated. Analysis shows that TI-S is positively correlated to gradient Richardson number Ri , and RE of ZS14 is increasing with the magnitude of Richardson number Ri under convection predominant unstable condition associating weak winds and strong vertical motion (Fig. A3). The
330 relationship between Ri and TI-S needs further study. Consequently, the results illustrate that the modified scheme $V_{d,\tau}$ tends to be more accurate than the unmodified scheme $V_{d,\tau}$.

4. Conclusion

The present study was designed to determine the effect of ABL stability on dust particle deposition. For this purpose, the WRF-LES/D was used to model atmospheric boundary-layer turbulence under the presence of
335 atmospheric stability effects to recover statistics of shear stress variability. We then presented an improved dust-deposition scheme with the consideration of turbulent shear stress. While ABL can broadly represent levels of atmospheric turbulence, its effect on dust deposition is wind speed dependent. Through a series of numerical experiments, we have shown the turbulent characteristics of dust deposition velocity caused by the turbulent wind flow and pointed out existing dust-deposition schemes have deficiencies in representing dust
340 deposition under convective conditions. The relative error RE increases as the ABL instability increases for low wind conditions, i.e., RE increases with shear stress turbulence intensity, especially for a certain size range of particles.

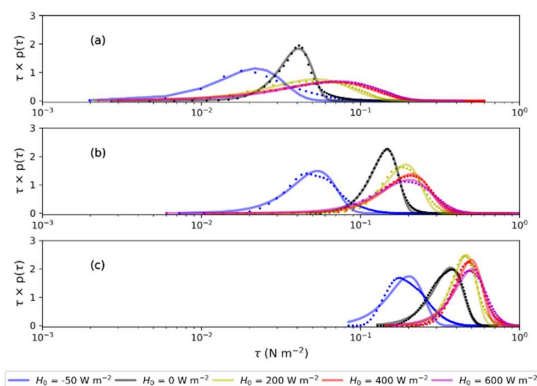
Since the dependency of dust deposition on micrometeorology is imbedded in the application of the surface shear stress, we believe that the dependency of dust deposition on ABL stability is ultimately attributed to
345 the statistical behavior of shear stress τ . Therefore, in this study, a model including the effects of surface shear fluctuations is proposed and validated by numerical experiments. Additionally, the fluctuations of surface shear caused by turbulence are available to estimate by a Weibull distribution function. The shape parameter decreases exponentially with the reciprocal of Monin-Obukhov length, and the scale parameter increases linearly with $u_{*r}^2 + 0.001w_*^2$. After statistically revising the original scheme, an improved model is obtained.



350 Using the modified model, the deposition velocity tends towards numerical experimental results.
 The project is the first comprehensive investigation of the turbulent characters of dust deposition and the findings will be of interest to improve the accuracy of dust-deposition predictions in regional or global scales. One source of weakness in this study is the variation of τ may change with surface roughness and needs further study. In spite of this limitation, the study adds to our understanding of the influence caused by ABLs
 355 on particle deposition.

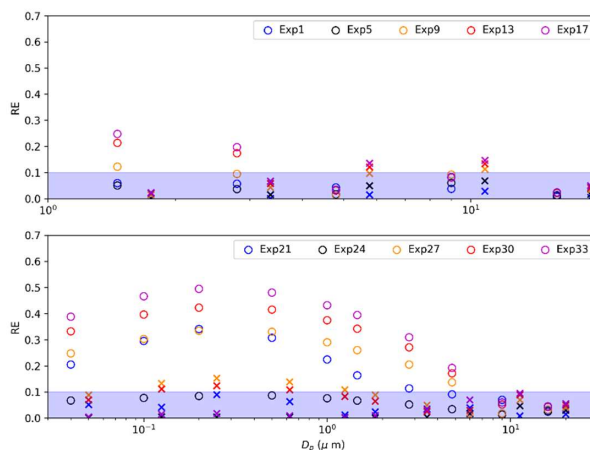
Appendix

Figure A1 shows the probability density distribution of surface shear stress for experiments (21-35); Figure A2 shows the changing of relative error with particle size; Figure A3 shows the variation of relative error (RE) of the ZS14 scheme (Eq. (10)) and improved scheme (Eq. (21)) with gradient Richardson number Ri .



360

Figure A1. Probability distributions of simulated surface shear stress (dots) and the corresponding fitted Weibull density distribution (solid lines) with different surface heat flux for different wind conditions: **(a)** $U = 5.44 \text{ m s}^{-1}$, **(b)** $U = 10.87 \text{ m s}^{-1}$, **(c)** $U = 18.12 \text{ m s}^{-1}$.





365

Figure A2. *RE* changes with particle size under weak wind conditions.

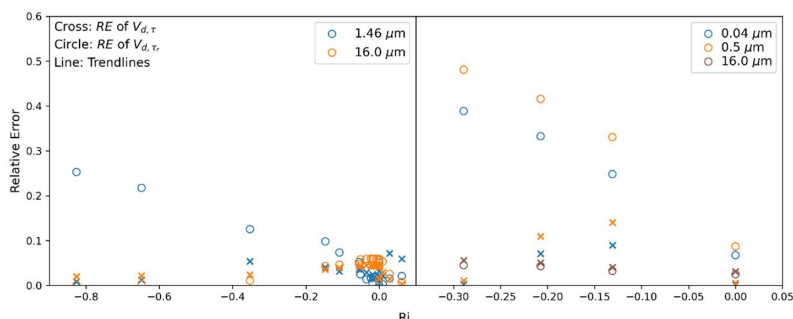


Figure A3. Comparison of relative error as a function of Ri , estimated by ZS14 scheme (circles) and the improved scheme (crosses) for Exp (1-20) (left) and Exp (24, 27, 30, 33) (right).

370 Code and data availability

The source code used in this study is the WRF-chem version 3.7 in the LES mode coupled with a new deposition scheme. WRF-LES model can be download at https://www2.mmm.ucar.edu/wrf/users/download/get_sources.html. The code of the coupled deposition scheme and data set obtained by the simulation are available online at <https://github.com/YinXin2021/WRF-LES-DustDepositionScheme>.

375

Author contributions

XY, YPS and JZ were responsible for the formal analysis, Methodology. XY and CJ were responsible for the data curation, software, validation and visualization. YPS, JZ and NH were responsible for the supervision, project administration and funding acquisition. XY was responsible for investigation and Writing - original draft preparation. XY, YPS and JZ were responsible for the Writing - review & editing.

380

Competing interests

The authors declare that they have no conflict of interest.

Disclaimer

Publisher's note: Copernicus Publications remains neutral with regard to jurisdictional claims in published maps and institutional affiliations.

385



Acknowledgments.

We thank the Second Tibetan Plateau Scientific Expedition and Research Program (2019QZKK020611), the State Key Program of the National Natural Science Foundation of China (41931179), the China Scholarship Council (No. 201606180041) and the Fundamental Research Funds for the Central Universities (grant no. lzujbky-2020-cd06).

References

- Bergametti, G., Marticorena, B., Rajot, J. L., Foret, G., Alfaro, S. C. and Laurent, B.: Size-Resolved Dry Deposition Velocities of Dust Particles: In Situ Measurements and Parameterizations Testing, *J. Geophys. Res. Atmos.*, 123(19), 11,080–11,099, doi:10.1029/2018JD028964, 2018.
- 395 Chamberlain, A. C.: Aspects of travel and deposition of aerosol and vapour clouds, U.K., <https://www.osti.gov/biblio/4406948>, 1953.
- Chamberlain, A. C.: Transport of Lycopodium spores and other small particles to rough surfaces, *Proc. R. Soc. London. Ser. A. Math. Phys. Sci.*, 296, 45–70, doi:10.1098/rspa.1967.0005, 1967.
- Chen, S. H. and Dudhia, J.: Annual report: WRF physics, Air Force Weather Agency, (January 2000), 1–38,
- 400 2000.
- Colella, K. J. and Keith, W. L.: Measurements and scaling of wall shear stress fluctuations, *Exp. Fluids*, 34(2), 253–260, doi:10.1007/s00348-002-0552-2, 2003.
- Connan, O., Pellerin, G., Maro, D., Damay, P., Hébert, D., Roupsard, P., Rozet, M. and Laguionie, P.: Dry deposition velocities of particles on grass: Field experimental data and comparison with models, *J. Aerosol Sci.*, 126(November 2017), 58–67, doi:10.1016/j.jaerosci.2018.08.004, 2018.
- 405 Csanady, G. T.: Turbulent Diffusion of Heavy Particles in the Atmosphere, *J. Atmos. Sci.*, 20, 201–208, doi:10.1175/1520-0469(1964)021<0322:codohp>2.0.co;2, 1963.
- Damay, P. E., Maro, D., Coppalle, A., Lamaud, E., Connan, O., Hébert, D., Talbaut, M. and Irvine, M.: Size-resolved eddy covariance measurements of fine particle vertical fluxes, *J. Aerosol Sci.*, 40(12), 1050–1058,
- 410 doi:10.1016/j.jaerosci.2009.09.010, 2009.
- Deardorff, J. W.: Stratocumulus-capped mixed layers derived from a three-dimensional model, *Boundary-Layer Meteorol.*, 18(4), 495–527, doi:10.1007/BF00119502, 1980.
- Droppo, J. G.: Improved Formulations for Air-Surface Exchanges Related to National Security Needs: Dry Deposition Models., Richland, WA., 2006.
- 415 Dudhia, J.: A multi-layer soil temperature model for MM5, Prepr. from Sixth PSU/NCAR Mesoscale Model Users' Work. 22-24 July 1996, Boulder, Color., 1996.
- Hicks, B. B., Saylor, R. D. and Baker, B. D.: Dry deposition of particles to canopies-A look back and the road forward, *J. Geophys. Res.*, 121(24), 14691–14707, doi:10.1002/2015JD024742, 2016.



- Ito, J., Niino, H. and Nakanishi, M.: Large eddy simulation on dust suspension in a convective mixed layer, *Sci. Online Lett. Atmos.*, 6(1), doi:10.2151/sola.2010-034, 2010.
- 420 Kalitzin, G., Medic, G. and Templeton, J. A.: Wall modeling for LES of high Reynolds number channel flows: What turbulence information is retained?, *Comput. Fluids*, 37(7), 809–815, doi:10.1016/j.compfluid.2007.02.016, 2008.
- Kawai, S. and Larsson, J.: Wall-modeling in large eddy simulation: Length scales, grid resolution, and accuracy, *Phys. Fluids*, 24(1), doi:10.1063/1.3678331, 2012.
- 425 Kind, R. J.: One-dimensional aeolian suspension above beds of loose particles-A new concentration-profile equation, *Atmos. Environ. Part A, Gen. Top.*, 26(5), 927–931, doi:10.1016/0960-1686(92)90250-O, 1992.
- Klose, M. and Shao, Y.: Stochastic parameterization of dust emission and application to convective atmospheric conditions, *Atmos. Chem. Phys.*, 12(16), 7309–7320, doi:10.5194/acp-12-7309-2012, 2012.
- 430 Klose, M. and Shao, Y.: Large-eddy simulation of turbulent dust emission, *Aeolian Res.*, 8, 49–58, doi:10.1016/j.aeolia.2012.10.010, 2013.
- Klose, M., Shao, Y., Li, X., Zhang, H., Ishizuka, M., Mikami, M. and Leys, J. F.: Further development of a parameterization for convective turbulent dust emission and evaluation based on field observations, *J. Geophys. Res.*, 119(17), 10441–10457, doi:10.1002/2014JD021688, 2014.
- 435 Klose, M. R.: Convective Turbulent Dust Emission : Process , parameterization , and relevance in the Earth system, 2014.
- Kosovic, B.: Subgrid-scale modelling for the large-eddy simulation of high-Reynolds-number boundary layers, *J. Fluid Mech.*, 336, 151–182, doi:10.1017/S0022112096004697, 1997.
- Lamaud, E., Chapuis, A., Fontan, J. and Serie, E.: Measurements and parameterization of aerosol dry deposition in a semi-arid area, *Atmos. Environ.*, 28(15), 2461–2471, doi:10.1016/1352-2310(94)90397-2, 1994.
- 440 Li, G., Zhang, J., Herrmann, H. J., Shao, Y. and Huang, N.: Study of Aerodynamic Grain Entrainment in Aeolian Transport, *Geophys. Res. Lett.*, 47(11), doi:10.1029/2019GL086574, 2020a.
- Li, G., Zhang, J., Herrmann, H. J., Shao, Y. and Huang, N.: Study of Aerodynamic Grain Entrainment in Aeolian Transport, *Geophys. Res. Lett.*, 47(11), 0–2, doi:10.1029/2019GL086574, 2020b.
- 445 Liu, D., Ishizuka, M., Mikami, M. and Shao, Y.: Turbulent characteristics of saltation and uncertainty of saltation model parameters, *Atmos. Chem. Phys.*, 18(10), 7595–7606, doi:10.5194/acp-18-7595-2018, 2018.
- Mirocha, J. D., Lundquist, J. K. and Kosović, B.: Implementation of a nonlinear subfilter turbulence stress model for large-eddy simulation in the advanced research WRF model, *Mon. Weather Rev.*, 138(11), doi:10.1175/2010MWR3286.1, 2010.
- 450 Moeng, C.-H., Dudhia, J., Klemp, J. and Sullivan, P.: Examining Two-Way Grid Nesting for Large Eddy Simulation of the PBL Using the WRF Model, *Mon. Weather Rev.*, 135(6), 2295–2311, doi:10.1175/MWR3406.1, 2007.



- 455 Monahan, A. H.: The probability distribution of sea surface wind speeds. Part I: Theory and SeaWinds observations, *J. Clim.*, 19(4), 497–520, doi:10.1175/JCLI3640.1, 2006.
- Monin, A. S.: The Atmospheric Boundary Layer, *Annu. Rev. Fluid Mech.*, 2(1), 225–250, doi:10.1146/annurev.fl.02.010170.001301, 1970.
- Monin, A. S. and Obukhov, A. M.: Basic Laws of Turbulence Mixing in the Ground Layer of the Atmosphere, *Tr. Akad. Nauk. SSSR Geophys. Inst.*, 24(151), 1954.
- 460 Monin, A. S., I?A?glom, A. M. and Lumley, J. L.: *Statistical Fluid Mechanics: Mechanics of Turbulence*, Dover Publications. [online] Available from: https://books.google.de/books?id=EtTyyI4%5C_DvIC, 2007.
- Pellerin, G., Maro, D., Damay, P., Gehin, E., Connan, O., Laguionie, P., Hébert, D., Solier, L., Boulaud, D., Lamaud, E. and Charrier, X.: Aerosol particle dry deposition velocity above natural surfaces: Quantification according to the particles diameter, *J. Aerosol Sci.*, 114, 107–117, doi:10.1016/j.jaerosci.2017.09.004, 2017.
- 465 Petroff, A. and Zhang, L.: Development and validation of a size-resolved particle dry deposition scheme for application in aerosol transport models, *Geosci. Model Dev.*, doi:10.5194/gmd-3-753-2010, 2010.
- Piomelli, U., Balaras, E., Squires, K. D. and Spalart, P. R.: Zonal approaches to wall-layer models for large-eddy simulations, in *3rd Theoretical Fluid Mechanics Meeting.*, 2002.
- Pleim, J. E. and Xiu, A.: Development of a land surface model. Part II: Data assimilation, *J. Appl. Meteorol.*, 42(12), 1811–1822, doi:10.1175/1520-0450(2003)042<1811:DOALSM>2.0.CO;2, 2003.
- 470 Rana, S., Anderson, W. and Day, M.: Turbulence-Based Model for Subthreshold Aeolian Saltation, *Geophys. Res. Lett.*, 47(15), 1–9, doi:10.1029/2020GL088050, 2020.
- Robinson, S. K.: Coherent motions in the turbulent boundary layer, *Annu. Rev. Fluid Mech.*, 23(1), doi:10.1146/annurev.fl.23.010191.003125, 1991.
- 475 Schmel, G. A.: Particle and gas dry deposition: A review, *Atmos. Environ.*, 14(9), 983–1011, doi:10.1016/0004-6981(80)90031-1, 1980.
- Seinfeld, J. H., Bretherton, C., Carslaw, K. S., Coe, H., DeMott, P. J., Dunlea, E. J., Feingold, G., Ghan, S., Guenther, A. B., Kahn, R., Kraucunas, I., Kreidenweis, S. M., Molina, M. J., Nenes, A., Penner, J. E., Prather, K. A., Ramanathan, V., Ramaswamy, V., Rasch, P. J., Ravishankara, A. R., Rosenfeld, D., Stephens, G. and
- 480 Wood, R.: Improving our fundamental understanding of the role of aerosol–cloud interactions in the climate system, *Proc. Natl. Acad. Sci.*, 113(21), 5781–5790, doi:10.1073/PNAS.1514043113, 2016.
- Shao, Y.: Simplification of a dust emission scheme and comparison with data, *J. Geophys. Res. D Atmos.*, 109(10), 1–6, doi:10.1029/2003JD004372, 2004.
- Shao, Y., Liu, S., Schween, J. H. and Crewell, S.: Large-Eddy Atmosphere-Land-Surface Modelling over
- 485 Heterogeneous Surfaces: Model Development and Comparison with Measurements, *Boundary-Layer Meteorol.*, 148(2), 333–356, doi:10.1007/s10546-013-9823-0, 2013.
- Shao, Y., Zhang, J., Ishizuka, M., Mikami, M., Leys, J. and Huang, N.: Dependency of particle size distribution at dust emission on friction velocity and atmospheric boundary-layer stability, *Atmos. Chem. Phys.*, 20(21), 12939–12953, doi:10.5194/acp-20-12939-2020, 2020.



- 490 Skamarock, W. C., Klemp, J. B., Dudhi, J., Gill, D. O., Barker, D. M., Duda, M. G., Huang, X.-Y., Wang, W. and Powers, J. G.: A Description of the Advanced Research WRF Version 3, Tech. Rep., (June), 113, doi:10.5065/D6DZ069T, 2008.
- Slinn, S. A. and Slinn, W. G. N.: Predictions for particle deposition on natural waters, *Atmos. Environ.*, 14(9), 1013–1016, doi:10.1016/0004-6981(80)90032-3, 1980.
- 495 Slinn, W. G. N.: Predictions for particle deposition to vegetative canopies, *Atmos. Environ.*, 16(7), 1785–1794, doi:10.1016/0004-6981(82)90271-2, 1982a.
- Slinn, W. G. N.: Predictions for particle deposition to vegetative canopies, *Atmos. Environ.*, doi:10.1016/0004-6981(82)90271-2, 1982b.
- Wesely, M. L., Cook, D. R. and Hart, R. L.: Fluxes of gases and particles above a deciduous forest in wintertime, *Boundary-Layer Meteorol.*, 27(3), 237–255, doi:10.1007/BF00125000, 1983.
- 500 Wesely, M. L., Cook, D. R. and Hart, R. L.: Measurements and parameterization of particulate sulfur dry deposition over grass., *J. Geophys. Res.*, doi:10.1029/jd090id01p02131, 1985.
- Wyngaard, J. C. (2010). Turbulence in the atmosphere. In *Turbulence in the Atmosphere*. <https://doi.org/10.1017/CBO9780511840524>
- 505 Yang, Y. and Shao, Y.: A scheme for scalar exchange in the urban boundary layer, *Boundary-Layer Meteorol.*, 120(1), 111–132, doi:10.1007/s10546-005-9033-5, 2006.
- Zhang, J. and Shao, Y.: A new parameterization of particle dry deposition over rough surfaces, *Atmos. Chem. Phys.*, 14(22), 12429–12440, doi:10.5194/acp-14-12429-2014, 2014.
- Zhang, L., Gong, S., Padro, J. and Barrie, L.: A size-segregated particle dry deposition scheme for an atmospheric aerosol module, *Atmos. Environ.*, doi:10.1016/S1352-2310(00)00326-5, 2001.
- 510 Zheng, X., Jin, T. and Wang, P.: The Influence of Surface Stress Fluctuation on Saltation Sand Transport Around Threshold, *J. Geophys. Res. Earth Surf.*, 125(5), 0–2, doi:10.1029/2019JF005246, 2020.